Effect of pre-treatment method on the nanostructure and performance of supported Co catalysts in Fischer-Tropsch synthesis

Robert W. Mitchell, [1,4] David C. Lloyd,[1,4] Leon van de Water,[5] Peter R. Ellis,[6] Kirsty A. Metcalfe,[7] Connor Sibbald,[7] Laura H. Davies,[7] Dan I. Enache,[7 *] Gordon J. Kelly, [7] Edward D. Boyes [1,3,4 *] and Pratibha L. Gai [1,2,4 *]

[1]*Departments of Physics, [2]Chemistry, [3]Electronics, and [4] The York JEOL Nanocentre, University of York, Heslington, York, YO10 5DD, UK*

[5] *Johnson Matthey Technology Centre, Belasis Ave, Stockton-on-Tees, Billingham TS23 1LH, UK*

[6] *Johnson Matthey Technology Centre, Blounts Court, Sonning Common, RG4 9NH, UK*

[7] *Johnson Matthey, Belasis Ave, Stockton-on-Tees, Billingham TS23 1LH, UK*

Abstract

Understanding precursor transformation to active catalysts is crucial to heterogeneous Fischer-Tropsch (FT) catalysis directed towards production of hydrocarbons for transportation fuels. Despite considerable literature on FT catalysis, the effect of pre-treatment of supported cobalt catalysts on cobalt dispersion, dynamic atomic structure and the activity of the catalysts is not well understood. Here we present systematic studies into the formation of active catalyst phases in supported Co catalyst precursors in FT catalysis using *in-situ* environmental (scanning) transmission electron microscopy (E(S)TEM) with single atom resolution under controlled reaction environments for *in-situ* visualization, imaging and analysis of reacting atomic species in real time, EXAFS, XAS, DRIFTS analyses and catalytic activity measurements. We have synthesized and analyzed dried-reduced (D) and dried-calcined reduced (DC) Co real catalysts on reducible and non-reducible supports, such as SiO_2, Al_2O_3, TiO_2 and ZrO_2. Comparisons of dynamic *in-situ* atomic structural observations of reacting single atoms, atomic clusters and nanoparticles of Co, DRIFTS, XAS, EXAFS and catalytic activity data of the D and DC samples reveal in most cases better dispersion in the D samples, leading to a larger number of low-coordination Co^0 sites and a higher number of active sites for CO adsorption. The experimental findings on the degree of reduction of D and DC catalysts on reducible and non-reducible supports and correlations between hexagonal (hcp) Co sites and the activity of the catalysts generate structural insights into the catalyst dynamics, important to the development of efficient FT catalysts.

1. INTRODUCTION

To address the world-wide demand for chemicals feed-to-liquids (referred to as XTL) technologies are being explored as a method to generate hydrocarbons from carbon feedstocks [1]. XTL is a three-step process, consisting of the reforming step that transforms the natural gas, coal, biomass, waste (etc.) into syngas, followed by the Fischer-Tropsch (FT) conversion, in which the syngas is transformed into long chain hydrocarbons and finally by the product upgrading, which is essentially a hydrocracking and/or isomerization step. Despite being nearly 100 years old [2], the catalysts used in (FT) synthesis are still being optimized by the industry and have received considerable worldwide attention [3-17]. The FT process can be performed over catalysts containing Fe, Co or Ru, with the supported Co-based catalysts being preferred because of their higher activity, lower selectivity to CO_2 and higher stability with time on line when compared with the Fe ones, or because of the lower cost when compared with the Ru-based products [3,4]. Liquid fuels derived from FT synthesis are free of S compounds and aromatic hydrocarbons, resulting in products that exceed all future specifications, allowing a drastic reduction of the particulate emissions and the elimination of the SO_x problem that diesel engines currently have. The absence of SOx should also allow the catalytic converters to deal more efficiently with the NOx emissions.

However, the effect of the pre-treatment of the supported cobalt catalysts on the catalyst dispersion, the dynamic atomic structure, and performance of the catalysts in FT catalysis is not well understood. FT catalyst activity and selectivity are reported to be dependent on several factors [18,19] including the nature of the Co, the catalyst support and synthesis method and it is reported that metallic Co plays an important role. Metallic cobalt can exist in two crystallographic structures, namely, the hexagonal close-packed (hcp) phase and the face-centred cubic (fcc) phase. In

nanometre scale particles, both hcp and fcc forms may coexist leading to structural defects such as stacking faults. The fcc structure is thermodynamically preferred above 450 °C whereas the hcp phase is favored at lower temperatures [20]. However, it is difficult to extract from the literature a clear picture of the effect of pre-treatment on the nanostructure and the specific effect of the crystal structure important in FT activity, selectivity and catalyst lifetime. Many parameters can influence the crystal structure, such as the support [21,22]; formulation [23, 24], thermal history [25], activation procedures[26-28] and promoters [29].

A recent modelling paper reports calculations of reaction rates for CO dissociation by Density Functional Theory (DFT) [30]. The results reported in this theoretical study suggest that the hcp Co presents a higher intrinsic activity than the fcc Co and its distinct crystallographic structure exposes a higher number of active sites. Moreover, according to the calculations, hcp Co favors the direct dissociation of CO, whereas fcc Co favors the hydrogen-assisted CO dissociation. These findings agree with the data published by van Santen et. al. [31] using a combined quantum-chemical modeling and micro-kinetics approach which states that direct CO activation is very sensitive to the structure of the surface and that only step-type structures provide activation energies low enough for this process to occur. The same study also states that the recombination with CH_2 species is more favorable on the stepped site than on a terrace, indicating the important role of low-coordination active sites associated with corners and edges of the Co particles in the reaction. These findings are supported by the CO-FTIR spectroscopy results published by Prieto et. al.[25], which crucially show that the activity of a catalyst is directly proportional with the density of low-coordination Co^0 sites, which are higher for samples with irregular metallic surfaces.

Experimental studies were also performed, trying to modify the fcc Co : hcp Co ratio. Davis et. al.[26] used Co carbidization of Co/SiO₂ catalysts, finding that hcp Co presents a 39% higher turnover frequency (TOF) when compared with fcc Co, while the selectivity to C_{5+} hydrocarbons was also improved. Khodakov et. al.[27] also used the Co carbidization technique on catalysts supported on alumina to change the fcc Co : hcp Co ratio. Their results show that the sample with the higher hcp : fcc ratio presents a Co time yield 50% higher than that of the sample containing the higher fcc Co amount. Significantly they found no change in the selectivity of the catalyst by the increase of the hcp Co at the expense of the fcc Co. Lynch et. al [32] used a combination of Co carbidization and reduction temperature profile to alter the fcc Co : hcp Co ratio on catalysts supported on SiO₂ and Al₂O₃. Their results also show that after the carbidization step (hcp Co rich sample), the sample supported on alumina presents a conversion rate that is 50% higher than that of the fcc Co-rich sample. For the silica-supported sample the increase in the activity of the carbidized sample is dramatically improved, showing a 3-fold increase. Enache et al.[9] used the direct reduction of the Co nitrate precursor opposed to the dried-calcined-reduced version of the catalyst supported on ZrO₂ as a method of changing the fcc Co : hcp Co ratio. Based on the ramp rate changes during the reduction step, the hcp Co-rich sample, obtained via the direct reduction of the precursor, achieved 50% to 100% increase in the value of the TOF. In all these cases, the selectivity is not affected by the change in the fcc Co : hcp Co ratio. In promoted Co-Re/ γ-alumina catalysts it is reported that H₂-CO-H₂ treatment showed benefits of hcp configurations of Co particles in FT activity [33].

In this study, we prepared and tested Co catalysts supported on the usual oxides used in FT applications: SiO₂, Al₂O₃, TiO₂ and ZrO₂. We used the drying-calcination-reduction (DC) versus the drying-reduction (D) methods to modify the fcc Co : hcp Co ratio in order to enhance our understanding of the effect of the pre-treatment method on the dispersion, the dynamic

nanostructure of the supported Co catalysts at the single atom resolution and on the performance of the catalysts in the applications. We combined a series of advanced characterisation techniques in an attempt to obtain deeper insights into the differences in activity (and eventually selectivity) generated by the catalyst dispersion and the variation of the fcc Co : hcp Co ratio.

2. EXPERIMENTAL SECTION

Materials, synthesis, methods and catalytic activity measurements. Co (20% by weight) was deposited onto SiO_2 (Cab-O-Sil M-S – 200 m^2/g), Al_2O_3 (Sasol Puralox HP14/150 – 150 m^2/g), TiO_2 (Evonik/Degussa P25 – 50 m^2/g) and ZrO_2 (MELCAT XZO01501/3 – 113 m^2/g) by incipient wetness impregnation of $Co(NO_3)_2.6H_2O$ ACS grade (Alfa Aesar) for alumina and silica supports and wet impregnation in the case of titania and zirconia. We deliberately chose to load the same amount of the active phase on all the supports studied, to have a direct comparison between the supports investigated. Samples were dried at 110 °C for 8 hours. The samples were then split, with half used as is and denoted as dried (D): D-Co/SiO_2, D-Co/Al_2O_3, D-Co/TiO_2 and D-Co/ZrO_2; and the other half calcined for 16 hours at 300 °C in air to give dried-calcined (DC) samples: DC-Co/SiO_2, DC-Co/Al_2O_3, DC-Co/TiO_2 and DC-Co/ZrO_2. All chemicals were used as received, without any prior purification or thermal treatment. The precursor D and DC samples were reduced *in-situ* in flowing hydrogen for 7 hours at 380 °C. After this the reactors were fed with the reaction mixture of H_2/CO/Ar for catalyst activity measurements. The experimental details of the measurements are described in the following sections and in the Supporting Information (SI).

Analyses

Analyses were carried out using the advanced techniques shown below, with details given in the SI.

XRD. K$_\alpha$ source (1.5406 Å), operated at a current of 40 mA and 40 kV voltage was employed. Data points were collected at 0.02° 2θ step intervals for 0.3 s/step.

Real time *in-situ* E(S)TEM imaging and analyses: Samples were gently pressed between two glass slides prior to deposition. Glass slides were used to gently break up clumps of dry catalyst sample prior to dispersion as powder, rather than using the sample in solution as alcohol or other solutions may re-disperse Co species by wetting the materials and alter the sample. The catalyst powder was dusted onto 5 nm carbon coated chips in a MEMS heating holder supplied by DENS solutions, where the coated carbon film is used to support the catalyst sample. Evolutions of atomic structural changes in the samples were visualized and analyzed *in-situ* using our in-house development of novel environmental (scanning) transmission electron microscope (E(S)TEM) in a modified double aberration corrected JEOL 2200FS, providing single atom resolution and full analytical functionalities under controlled reaction environments [34-38]. The E(S)TEM functionalities include HAADF (high angle annular dark field imaging for observing atomic number contrast, described in the SI), electron diffraction, energy dispersive X-ray (EDX) spectroscopy for composition and single atom imaging under controlled reaction environments in both ETEM and ESTEM under flowing reactive gas environments and operating temperatures [34-38]. The E(S)TEM extends the earlier pioneering development of *in-situ* atomic resolution-environmental TEM (atomic resolution-ETEM) of Boyes and Gai [39] which enables dynamic studies of gas-solid reactions at the atomic level under controlled realistic reaction environments at elevated temperatures (up to 1000 °C and higher) and gas pressures up to 50mbar [39,40]. The original

ETEM (of Boyes and Gai) [39] is exploited for commercial production and used worldwide [41]. In ESTEM gas pressures of ~ 2Pa used at the sample cover sample surfaces with many thousands of monolayers of gas per second and are found to be generally fully adequate to flood the sample surface with gas molecules and drive the chemical reaction [35-38]. Calibration experiments were carried out *in-situ* to limit and remove deleterious effects of the electron beam: by blanking the beam during reactions on samples and the beam was switched on to record the final reaction endpoint. The data were cross checked with *in-situ* experiments under low dose imaging conditions [40-46]. Under these careful conditions the evolution of the nanostructure in the EM reactor can be directly correlated to that under technological conditions [47,48]. Methods to identify single atoms reported in the literature were employed. Details are given in the SI.

DRIFTS and chemisorption analyses. DRIFTS spectra were recorded with a Thermo Scientific Nicolet NEXUS Impact 6700 FT-IR spectrometer equipped with a MCT-A detector cooled by liquid nitrogen. *In-situ* measurements were carried out in a ceramic sample holder equipped with a thermocouple that was in direct contact with the sample. The DRIFTS spectra presented in this study are obtained after admission of one pulse of 10%CO in nitrogen in the pure nitrogen stream and are the first recorded after the disappearance of the absorption band characteristic to free CO. The purpose of this study was not to investigate the kinetics (and dynamics) of the chemisorption of CO onto metallic Co, but to try to quantify the hcp:fcc ratio for each sample studied, assuming that the kinetic of adsorption of CO onto the two types of metallic Co is identical or at least similar. A quantitative analysis of the adsorbed CO onto the samples was not attempted in the present study, because the concentration of adsorbed CO species is unknown or determined with a very high error margins, making the calculation of the IR absorption coefficients an impossible task.

Hydrogen chemisorption measurements were performed for DC-samples only using a Micromeritics 2480 Chemisorb HTP chemisorption analyzer after reducing the samples at 380 °C, using the method described by Reuel and Bartholomew [49]. We attempted to perform the hydrogen chemisorption analysis also on D – samples. However, this proved difficult as the gas fumes generated during the reduction process made the seals in the Micromeritics equipment to leak. If the equipment is not air-tight, the results obtained are not accurate. The only way to be able to measure the Co surface area via the hydrogen chemisorption, is for the samples to be manipulated in air. That would involve R-O-R (Reduction-Oxidation-Reduction treatment) but that would change the sample and also the hcp:fcc ratio. Moreover, not every Co atom in the surface of the particle size is necessarily an active site for the FT synthesis reaction [31]. If that were the case, then the activity of all the catalysts would be just a function of Co surface area value, which clearly is not the case.

XAS analysis. Samples of the as-prepared catalyst precursors were reduced in flowing hydrogen at 380 °C for 7 hours, using a ramp rate of 1 °C/min. The reduced catalysts were transferred into a nitrogen glovebox without exposure to air. The samples were passivated by mixing with wax (Shell SX-70), followed by heating of the mixture to melt the wax. This had the effect of making the samples air-stable, allowing them to be manipulated freely. Details are described in the SI. Data were analysed using ATHENA and ARTEMIS software packages [50].

EXAFS data were analysed in k^3 space over the range 3-12 Å^{-1}. Three distances were fitted: Co-O at 1.9-2.1 Å, Co-Co for cobalt metal at 2.5 Å and a higher Co-Co shell of cobalt oxide at 3.0 Å. A degree of reduction measurement was calculated from EXAFS fitting using the formula:

$$DoR = x_{Co\text{-}Co,\ foil} / (x_{Co\text{-}O} + x_{Co\text{-}Co,\ foil})$$

where x_{Co-O} and $x_{Co-Co, foil}$ are the coordination numbers for Co-O from all species and Co-Co from metal respectively (SI).

Catalyst activity evaluations. The test rig employed for the evaluation consists of a system of 6 parallel silica-coated reactor tubes, each of them fed individually by a mass flow controller (SI). Unreacted gas and the volatile products pass through a gas-liquid separator heated at 100 °C, then through a gas-liquid separator cooled at 5 C. The permanent gases stream is then used by a back-pressure regulator to achieve the desired pressure in the system. Periodic samples of the gas phase are analysed using a Varian CP-3800 gas chromatograph, equipped with two TCD and one FID detectors. The GC data are used as soon as the analysis is finished to calculate the conversion levels and the selectivity to methane, C_2-C_4 hydrocarbons, CO_2 and the selectivity to C_{5+} hydrocarbons. Wax and liquid samples were collected from the gas-liquid separators at the end of the experiment and sent for off-line analysis, allowing the determination of the chain growth probability value (alpha) (SI). The catalysts were compared at iso-conversion level, to be able to compare at the same time the selectivity to products. Otherwise, the catalysts would be exposed to different gas composition, rendering the selectivity comparison prone to errors.

3. RESULTS

Catalytic activity data

Table 1 presents the catalytic results obtained with these catalysts between 100 and 120 hours of time on line and show that in all cases we have an increase in the activity of the catalysts by removing the calcination step with no detrimental effect over the selectivity of the process. The activity of the catalysts was calculated using the formula:

$$A = \frac{syngas\ conversion \times GHSV}{100}$$

(where GHSV is gas hourly space velocity).

The relative activity was calculated by dividing the activity values of each catalyst to lowest value activity measured in these series (DC-Co/ZrO$_2$). Values of CTY (Co-Time-Yield) were also calculated for each catalyst and are provided in Table 1. The data show that the ratios between CTY values are equivalent to the corresponding values of relative activity. Finally, a ratio of activity D/DC was calculated for each catalyst.

Table 1. Catalytic results obtained after 100 to 120 hours of time on line (average values of 5 experimental points)

Catalyst	Conv. Syngas /%	Conv. CO /%	S CH$_4$ /%	S C$_2$-C$_4$ /%	S C$_{5+}$ /%	CTY /10^{-5}mol$_{CO}$ g$_{CO}^{-1}$ s^{-1}	Relative activity	Ratio activity D/DC
DC-Co/SiO$_2$	47.3	43.8	8.3	1.8	89.9	6.75	2.44	1.59
D-Co/SiO$_2$	52.3	48.3	9.4	1.7	88.9	10.74	3.88	
DC-Co/Al$_2$O$_3$	46.5	42.3	13.1	2.8	84.0	6.93	2.50	1.41
D-Co/Al$_2$O$_3$	49.5	46.8	8.3	2.2	89.5	9.75	3.52	
DC-Co/TiO$_2$	51.3	46.5	9.1	2.0	88.9	2.79	1.01	2.51
D-Co/TiO$_2$	55.0	51.5	8.0	1.5	90.5	7.01	2.53	
DC-Co/ZrO$_2$	43.2	38.8	7.9	1.8	90.2	2.77	1.0	2.28
D-Co/ZrO$_2$	50.2	45.9	7.4	1.9	90.7	6.33	2.28	

The results in **Table 1** indicate that by dispensing with the calcination treatment, the performance of each catalyst improves compared to its DC counterpart. This modification of the activity is significant for the non-reducible supports (silica and alumina) with increases of ~40-60%, but is clearly striking on the reducible supports (titania and zirconia) with an increase of more than 100%.

The table further shows that in terms of the activity the non-reducible supported catalysts outperform those on reducible supports.

PXRD profiles of the DC samples show the presence of the pattern characteristic of the Co_3O_4 species and those related to the supports. Profiles for the D samples only show patterns related to the crystalline supports (alumina, titania and zirconia). These data are illustrated in the supporting information (SI) in **Figures S1-S4**. Structural models for Co and Co-oxide phases are shown in **Figure S5**.

Table 2 and **Figure S6** present results of Co_3O_4 crystallite sizes obtained using the Scherrer's equation as a function of BET surface area. Co surface area values were obtained using the hydrogen chemisorption method for dried-calcined samples.

Table 2. Co_3O_4 crystallite size measured via PXRD and Co surface area values measured using the hydrogen chemisorption method

| Catalyst	Support BET Surface area /m^2/g	Co_3O_4 crystallite size /nm	Co surface area /m^2/g
DC-Co/SiO$_2$	200	23.5	7.8
DC-Co/Al$_2$O$_3$	150	26.3	8.9
DC-Co/ZrO$_2$	113	35.1	6.2
DC-Co/TiO$_2$	50	45.7	1.6

The results in **Table 2** (and **Figure S6**) indicate that there is an inverse correlation between the size of the Co_3O_4 crystallites and the BET surface area of the support. This shows that the size of the Co_3O_4 crystallites is dependent on the density of the crystallites per nm^2 of the support and the average pore diameter, rather than the type of support employed. Moreover, the H_2 chemisorption results for the catalysts on reducible supports might also be affected by the presence of the hydrogen spillover phenomena [51]. **Figure S6** also demonstrates that the relative activity is not a

direct function of the Co surface area and that there is a second factor that influences the measured activity of the catalyst.

Dynamic *in-situ* ESTEM observations at the single atom resolution

We employed in-situ E(S)TEM to investigate the dynamic nature of Co species and the catalyst dispersion in the samples during hydrogen reduction. The Co/SiO_2 samples are the initial focus here as the irreducible and amorphous nature of the support simplify the analysis. Observations and analysis of $DC-Co/SiO_2$ and $D-Co/SiO_2$ during H_2 reduction were carried out and the samples were reduced at 400 and 500 °C for 7 hours. In the present experiments EDX analyses were carried out ex-situ in the STEM mode to indicate the distribution of Co species on the real support (of variable thickness) for D and DC samples. The temperatures were selected due to their relevance to industrial catalyst reduction temperatures. In $DC-Co/SiO_2$, following 5 hours of reduction in hydrogen a population of small particles was visible on the support illustrated in **Figure 1**, in areas away from large cobalt oxide particles (discussed in the following sections).

Figure 1(a) shows an ETEM transmission image of Co species, in which it is difficult to reliably observe Co atomic species against the support contrast. To reliably discern small Co species on the support, ESTEM-HAADF was therefore employed which unmasked reacting small Co atom clusters (< 1nm) and small nanoparticles (on average ~ 1 to 2 nm and some larger) of Co with irregular surfaces, as well as contrast indicative of single atoms of Co on the support under the reaction conditions. These are shown in **Figures 1(b)**, **(c)** and **(d)** even after 7 hours**,** illustrating the resolution benefits of the *in-situ* ESTEM in imaging dynamic atomic species reliably under the reaction conditions. **Figures 1(e)** and **(f)** show intensity profiles (from regions indicated in (d)) consistent with single atoms and clusters of Co (circled).
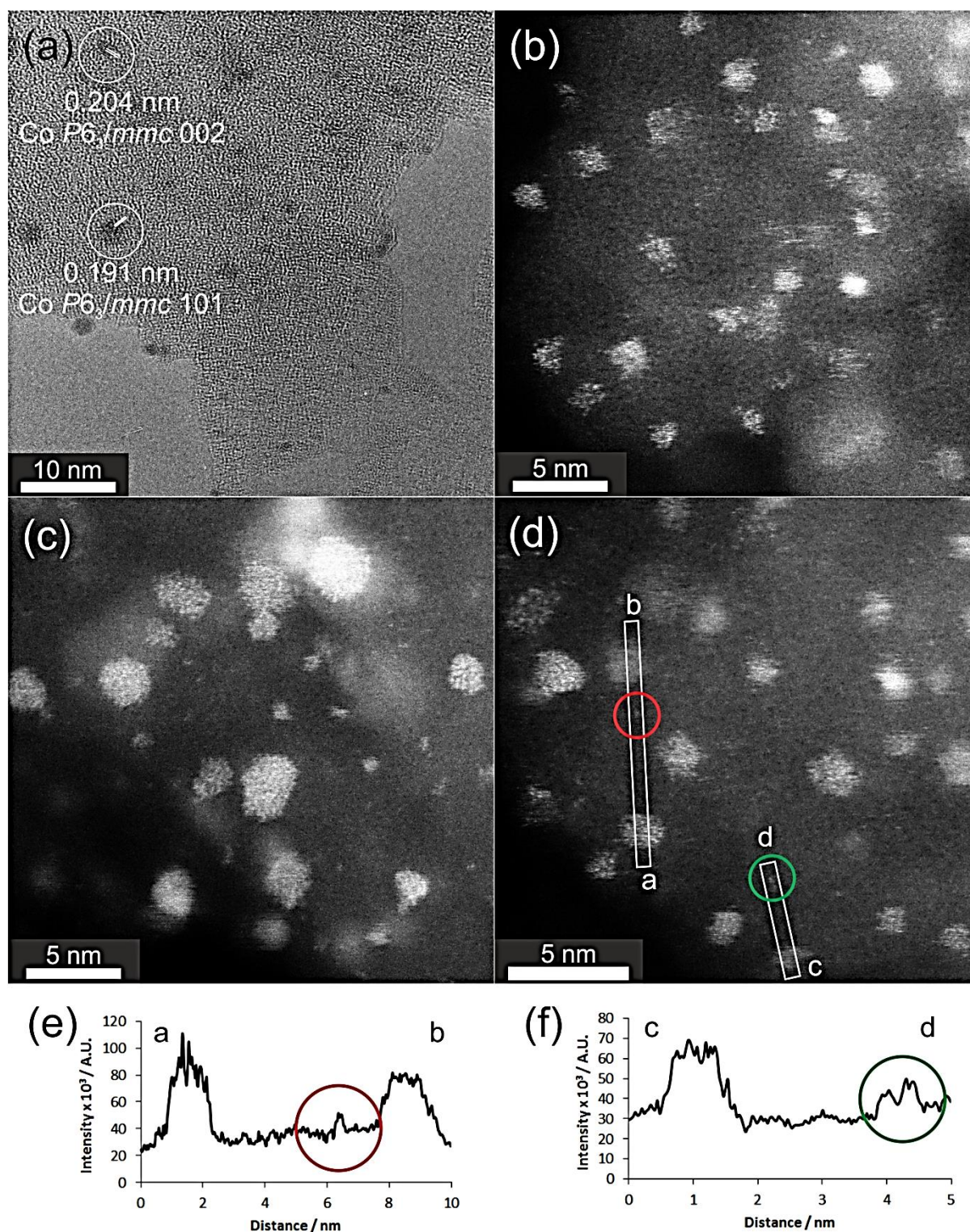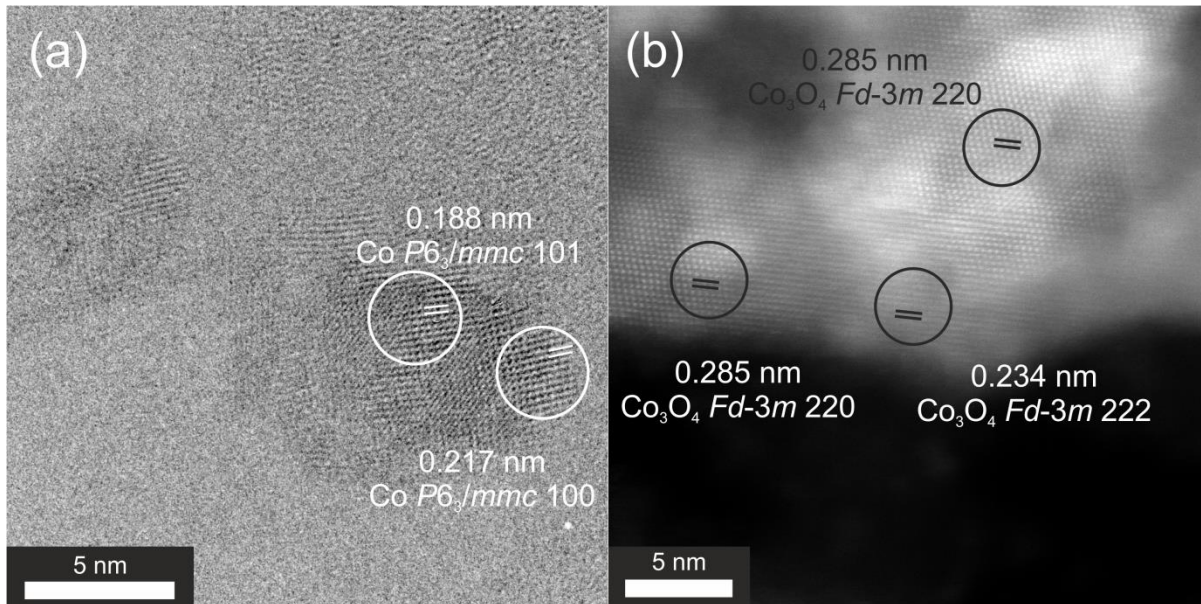
Figure 1: *In-situ* dynamic ETEM and ESTEM images at single atom resolution of *DC-Co/SiO₂* powder during 7 hours of reduction reaction in hydrogen at 400 °C. Lattice measurements from ETEM images in (a) are consistent with the hexagonal Co phase. Dynamic small clusters of Co (<1nm) and nanoparticles of Co with irregular surfaces and single atoms of Co are revealed in the

ESTEM images (b) – (d). (e) and (f) show intensity profiles of regions in (d), with deviation from the background noise consistent with clusters and atoms (circled).

Analyses of lattice spacings of the small Co particles during hydrogen reduction of the DC-Co/SiO$_2$ at 500 °C are shown in **Figure 2.** They reveal the presence of small hexagonal Co particles after 3h and the formation of some cubic Co after 7h.

Figure 2: *In-situ* dynamic (a) ETEM and (b) ESTEM images at the atomic level during 7h H$_2$ reduction of DC-Co/SiO$_2$ at 500 °C. (a) after 3 hours, small hexagonal Co particles are observed. After 7 hours some formation of the thermodynamically favored cubic Co phase is observed, while in (b) larger oxide particles remain unreduced.

After in-situ reduction for 3 hours, the DC-Co/SiO$_2$ sample contains both metallic and oxide species, as shown in **Figure 2(a)**. The metallic Co mostly appears to be in the form of hcp Co nanoparticles (space group: p6$_3$/mmc) (**Figure 2(a)**). After reduction for 7 hours the thermodynamically favored cubic Co phase is observed in agreement with the expected phase transformation from hexagonal to cubic above 450 °C. [20] However, the majority of the Co resides in the oxide species which take the form of large particles of Co$_3$O$_4$ (space group: Fd-3m) (**Figure**

2(b)). Some of these particles are partially reduced to CoO, as shown in **Figure S7** via selected area dynamic electron diffraction.

In contrast, the D-Co/SiO₂ sample during hydrogen reduction shows a greater and uniform population of the Co metal species throughout the sample, (with Co nanoparticles taking the form of hcp Co nanoparticles). Large cobalt oxide particles were not observed. The dynamic ESTEM sequence from the same area of the sample (near P) recorded at 2 min intervals to track reacting Co atomic species and nanoparticles during the hydrogen reduction at 400 °C for 7 h are shown in Figures 3 (a-c). Co atomic species and Co nanoparticles observed in (a) show redistribution of species and coalescence and growth of some nanoparticles during the reaction (shown in (c)). Figure 3 (d) shows the intensity profile consistent with a single atom (e.g. bright dot contrast) on the support near the arrow in (b), with details in the SI). The dynamic electron diffraction data during the hydrogen reduction at 400 °C for 5 and 7 hours are shown in **Figure 4(a)** and **(b)**, respectively, showing increasing crystallinity (and evolution of reflections) of Co species in **Figure 4(b)**. The areas near the arrow in Figure 3(b) are presented at higher magnification in Figure 4 (c) and (d) illustrating reacting small atomic clusters and single atoms of Co. The presence of Co atoms and atomic clusters of Co are clearly visible in the *in-situ* ESTEM images in Figures **3**, **4(c)** and **(d).**

The dynamic image sequence of the catalyst particles from the same larger area during the hydrogen reduction at 400 °C for 1,3,5 and 7 hours is shown in **Figure S8**, with the corresponding selected area dynamic electron diffraction patterns shown in **Figure S9**.
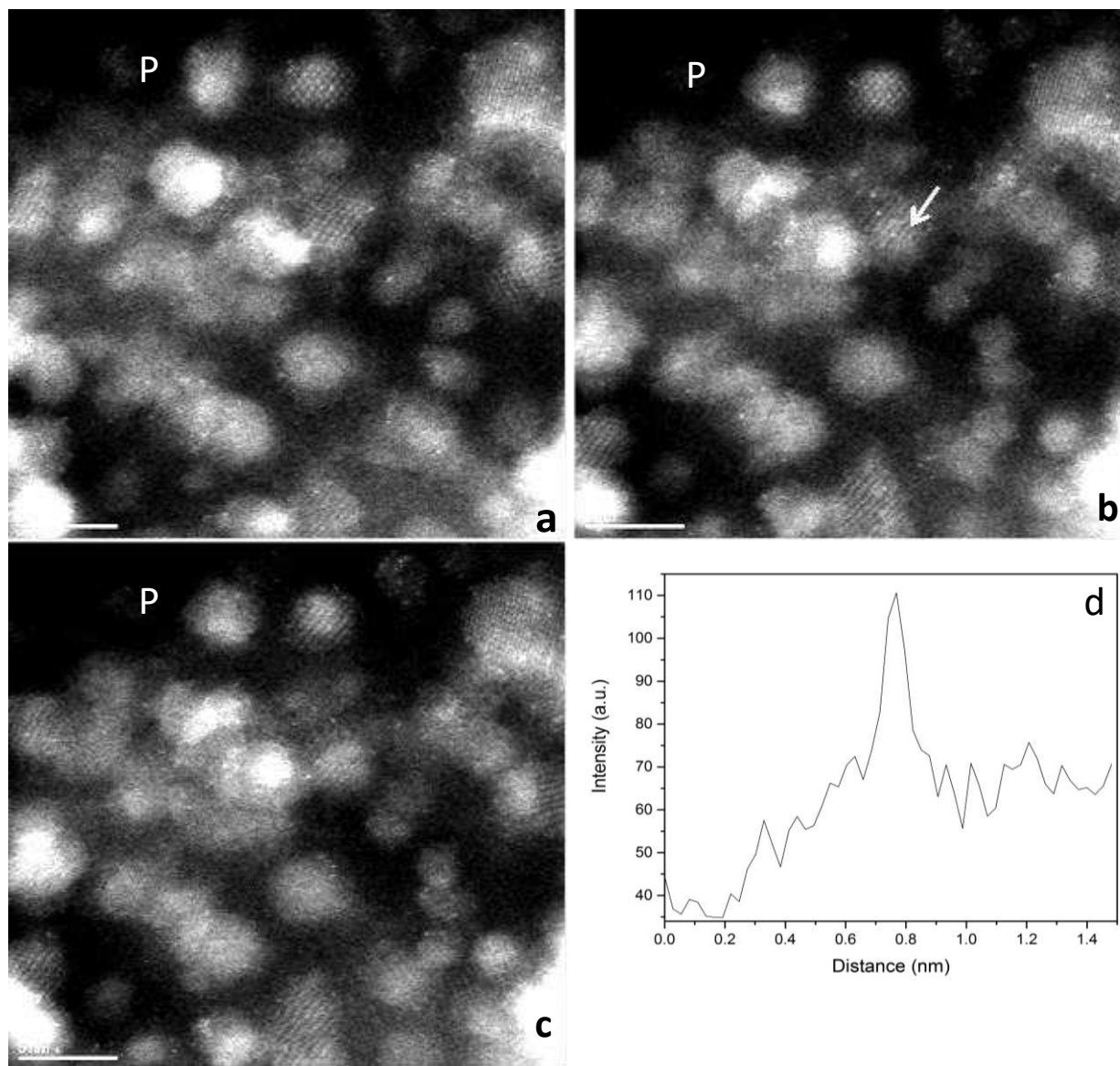
Figure 3 (a-c): Time resolved dynamic ESTEM image sequence recorded from the same area of the D-Co/SiO$_2$ sample (near P) tracks operating Co single atoms, atomic clusters and nanoparticles of Co on the real support during hydrogen reduction at 400 °C for 7h. Co atomic species and some Co nanoparticles observed in (a), show redistribution and growth of some nanoparticles (shown in (c)) during the reaction. (d) intensity profile from a single atom in the supported catalyst, (e.g. near the arrow in (b)). (The scale bar is 5nm).
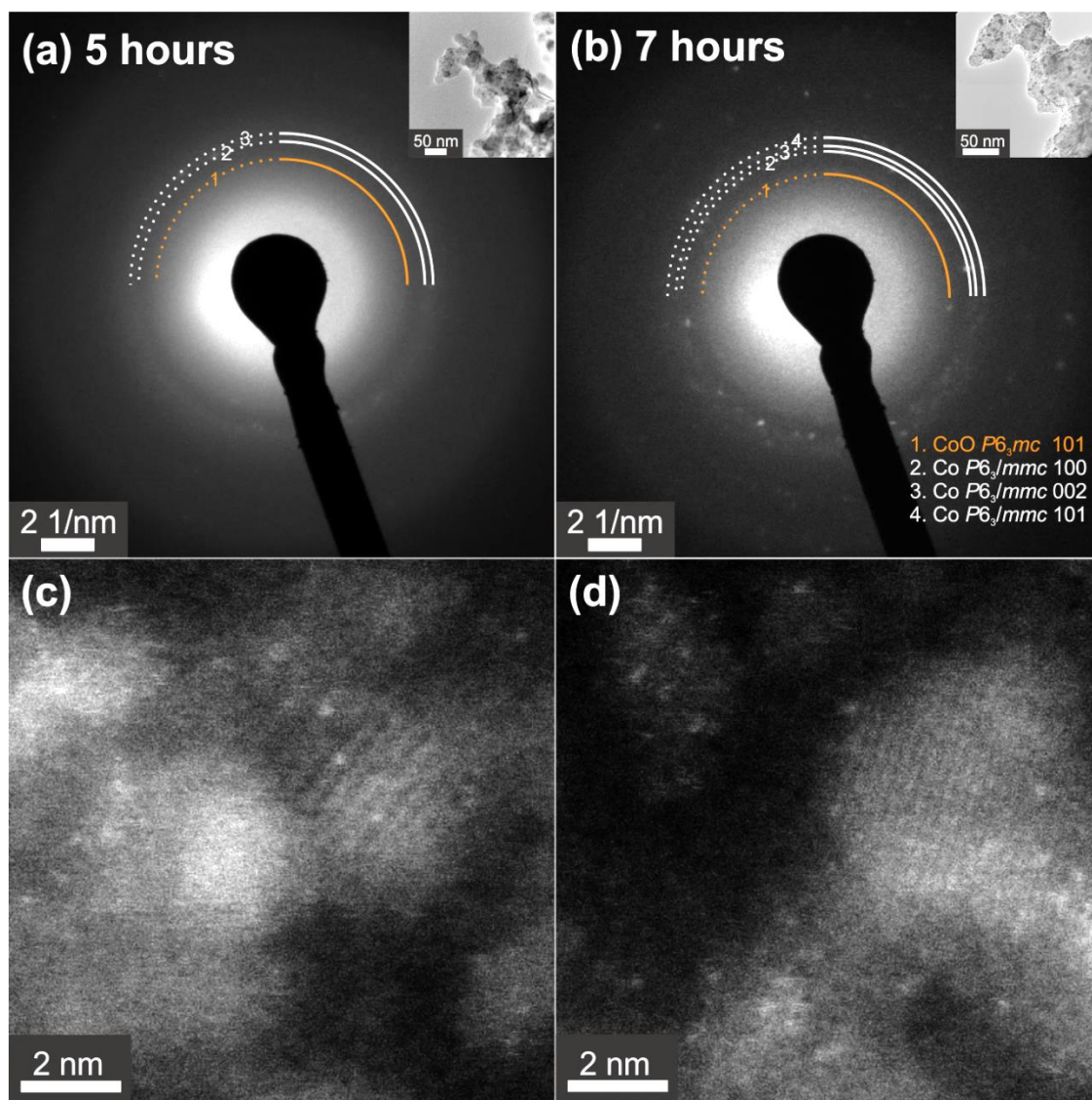
Figure 4: Dynamic selected area electron diffraction patterns recorded *in-situ* during the reduction of D-Co/SiO$_2$ at 400 °C. Diffraction patterns are displayed following: (a) 5 h and (b) 7 h of reduction and show increasing crystallinity of the Co species in (b); (e.g. reflections can be seen at the bottom of the pattern in (b). Insets show the selected sample areas for the patterns. (Scale bar for insets measures 50 nm). Higher magnification *in-situ* dynamic ESTEM-HAADF images (from an area near the arrow in Figure 3 (b)) during 7 hours H$_2$ reduction are shown in (c) and (d), revealing reacting small clusters and single atoms (bright dot contrast) of Co on the support during the reaction.

The higher dispersion of the Co species in D samples is supported by EDX composition analysis, shown in **Figure S10**. The D samples show generally uniform distribution of the Co species.

A comparison of the D and DC on SiO_2 supported samples after in-situ reduction are presented in

Figure 5. The comparison shows that the DC sample contains larger particles and clumps of Co

oxide particles. These large unreduced Co_3O_4 particles observed throughout the DC sample

reduce the metal surface area of the DC-Co/SiO_2 sample compared to the dried-only sample.
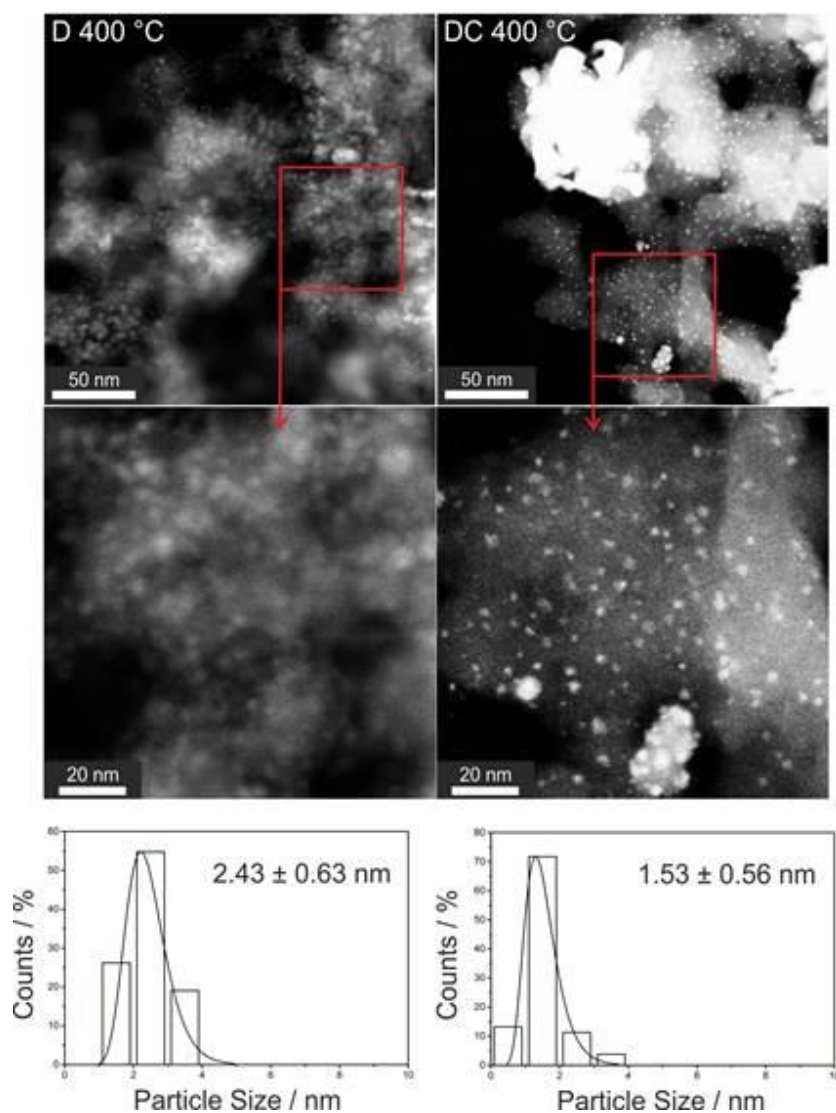
Figure 5: *In-situ* dynamic ESTEM images showing the general distribution and average Co particle sizes for D-Co/SiO_2 (left) and DC-Co/SiO_2 (right) at 400 °C in hydrogen gas. Large particles (clumps) of Co-oxide phases are present throughout the DC sample but not in the D sample, and these are not included in the particle size distribution (PSD).

Figure 5 also shows particle size distributions (PSDs) of the Co metal nanoparticles in both samples (excluding the larger Co oxide particles observed in the DC sample which reduce the metal surface area). The DC-Co/SiO$_2$ sample shows a smaller average particle size (~ 1.53 nm) than the equivalent experiment for D-Co/SiO$_2$ sample (~ 2.43 nm). These small particles would not be detectable by XRD since particles smaller than 3 nm are considered amorphous by XRD analysis. Hence, only large Co$_3$O$_4$ crystals are averaged to give the results presented in **Table 2**. Despite the larger Co particle size in the dried-only sample, the ESTEM images and the EDX analysis (**Figure S10**) show a better dispersion of the Co metal species.

Dynamic ESTEM studies were also performed to examine the effect of higher temperatures on the Co catalyst nanoparticles. There are reports that above the Tamman temperature of 611 °C sintering of the nanoparticles is expected due to increasing mobility of surface atoms [52]. Examples of dynamic in-situ ESTEM-HAADF observations from the same area of the sample, as a function of temperature and time, showing sintering of Co/SiO$_2$ during H$_2$ reduction are presented in **Figure S11**. The observations reveal Co nanoparticles undergoing a sintering process evidenced by a discernible decrease in the number of the nanoparticles following the reduction at 700 °C (d).

Comparison with in-situ E(S)TEM observations of Co/Al$_2$O$_3$, Co/TiO$_2$ and Co/ZrO$_2$.

To investigate the effect of the support on the active catalyst phase we compare and contrast the silica supported samples with those supported on alumina, titania and zirconia. **Figure 6** shows a comparison of the D and DC samples on the different supports. The images are recorded following 7 hours in-situ reduction at 400 °C in hydrogen. The strength of the interactions between CoO$_x$ species and the support influences the temperature required to reduce the metal. The interaction

between Co and alumina is expected to be stronger than that between Co and silica [4]. The alumina supported catalysts shown in **Figure 6(a)** and **(b)** appear similar to the silica supported catalysts. They also show a bimodal distribution in the DC-Co/Al$_2$O$_3$ with large agglomerates of Co and oxide phases. The dried-only sample shows a population of small <5nm particles. Dynamic electron diffraction reveals that even in the case of the DC-Co/Al$_2$O$_3$ some of the Co oxide species are reduced to the cubic Co metal (space group: Fm3m), as seen in **Figure S12**. EDX composition map showing bimodal distribution of Co species in Co/alumina is shown in **Figure S13**.

For the catalysts on reducible supports (titania and zirconia) the bimodal distribution of Co species is not observed and the samples show well dispersed discrete nanoparticles of Co. In the case of the titania supported samples (**Figure 6(c)** and **6(d)**), the Co species show a moderate dispersion on the support and discrete nanoparticles of Co can be clearly observed on the support. PSDs and EDX analysis are given in **Figures S14-S15**.   The Co nanoparticles in the D-Co/TiO$_2$ have an average size of 2.98 ± 0.15 nm, whereas the Co particle size is much larger at 9.82 ± 0.43 nm in the DC-Co/TiO$_2$. This tendency to a larger particle size is most likely due to the calcination step. Finally, the zirconia supported samples are shown in **Figure 6(e)** and **6(f)**, the D-Co/ZrO$_2$ sample supported very small nanoparticles of average size 1.8 ± 0.46 nm (shown in **Figure S16)**. However, during the in-situ reduction a high degree of Co migration off the support is observed during in-situ ESTEM. Whereas the DC-Co/ZrO$_2$ show a wider distribution of Co species and in some cases coalescence of the Co results in particles of the same size as the smallest zirconia crystallites, as such no PSD is given for this sample due to a larger uncertainty. A representative ESTEM image and EDX of the DC-Co/ZrO$_2$ sample is shown in **Figure S17**. HRTEM and selected area electron diffraction (SAED) data of D- Co/ZrO$_2$ are shown in **Figure S18.**
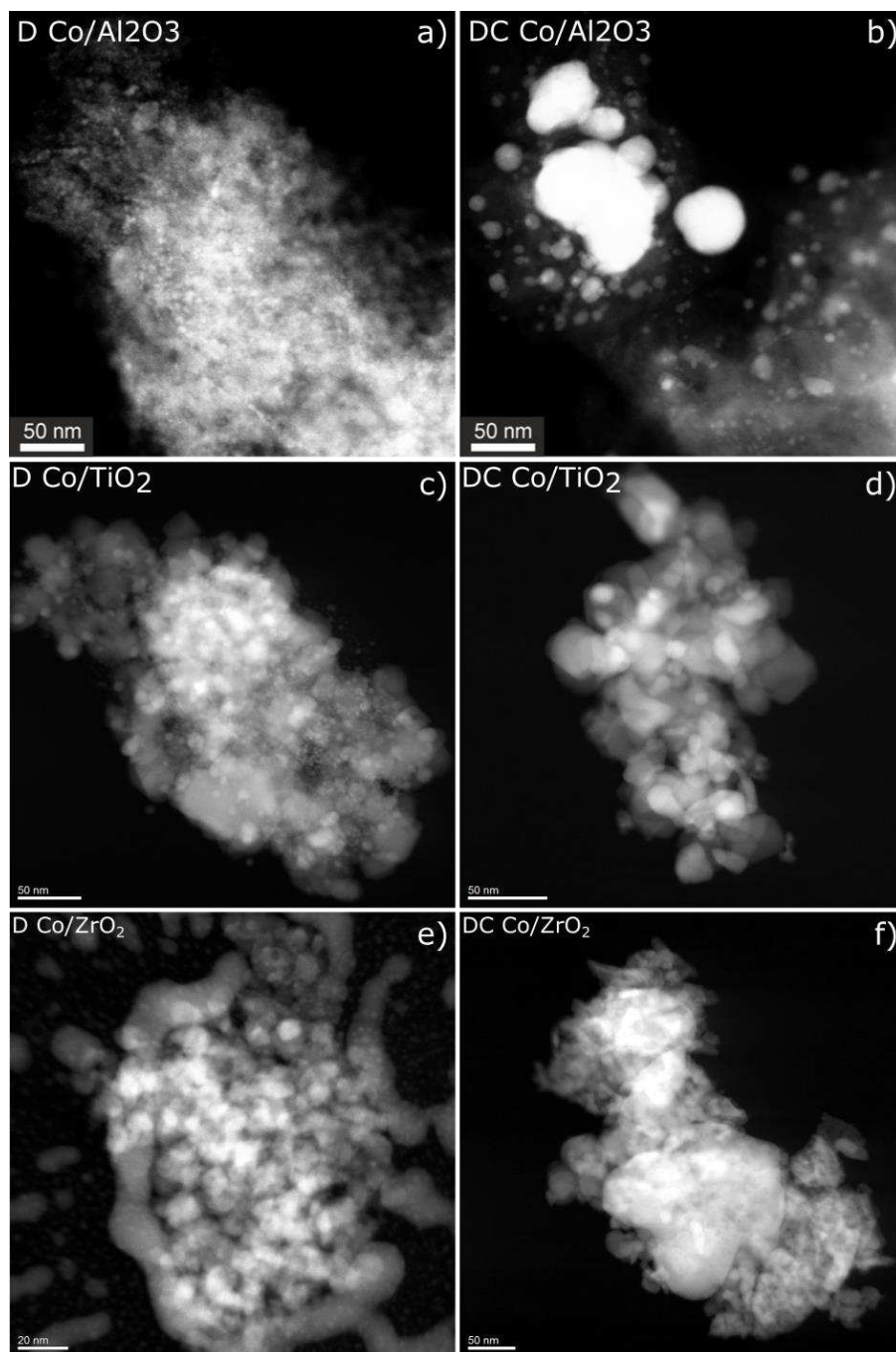
Figure 6: ESTEM-HAADF images illustrating the distribution of Co particles following H_2 reduction at 400 °C in (a) D-Co/Al_2O_3 and (b) DC-Co/Al_2O_3; (c) D-Co/TiO_2 and (d) DC-Co/TiO_2; (e) D-Co/ZrO_2 and (f) DC-Co/ZrO_2.

X-Ray absorption spectroscopy (XAS), XANES fitting and EXAFS

XAS data were acquired at the cobalt K edge for reduced and wax-encapsulated samples as described in the experimental section. XAS is an excellent method for assessment of degree of reduction in wax encapsulated catalysts where other techniques such as XRD or TPR (temperature-programmed reduction) are made more difficult due to the presence of the wax.
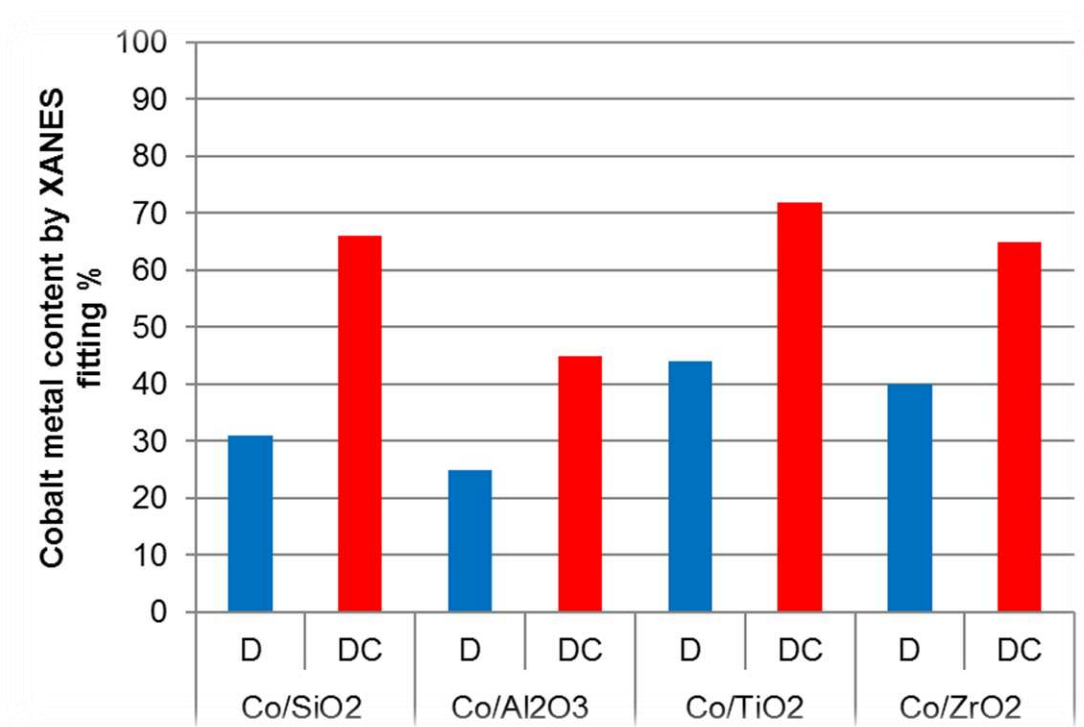
Figure 7: Degree of reduction measurements of D and DC Co catalysts derived from XANES fitting.

The XANES fitting, shown in **Figure 7**, revealed that all of the DC samples were more highly reduced than their D equivalents. During the calcination step sintering and oxidation of the Co species results in larger agglomerate clusters of oxide phases, which is consistent with the ESTEM results (**Figures 5** and **6**). These agglomerates of oxide phase lead to the greater degree of reduction as they are reduced (or partially reduced) to form metallic Co on the surface; while the bulk of the

agglomerates remain oxidized as shown earlier using electron diffraction. In contrast, the dried-only samples contain a much higher dispersion of the metal phase and show a lesser degree of reduction. These results are in strong agreement with previous results reported for Co/SiO_2 catalysts by Prieto et.al.[25].

Table 3. Results of EXAFS fitting / characterization. R=Co-O interatomic distance, ss = Debye – Waller factor and x = amount of phase present (the coordination number, on a scale 0 – 1)

Formulation	Co-O			Co-Co			%Co/(Co+CoO)
	R	X	Ss	R	x	ss	
D-20%Co/SiO$_2$	1.94	0.71	0.010	2.50	0.06	0.002	7.4
DC-20%Co/SiO$_2$	1.97	0.43	0.016	2.49	0.53	0.006	55.2
D-20%Co/Al$_2$O$_3$	1.93	0.77	0.009	2.51	0.06	0.005	7.2
DC-20%Co/Al$_2$O$_3$	2.00	0.64	0.014	2.50	0.33	0.006	34.0
D-20%Co/TiO$_2$	1.93	0.52	0.006	2.50	0.19	0.005	26.8
DC-20%Co/TiO$_2$	1.95	0.28	0.019	2.49	0.57	0.005	67.1
D-20%Co/ZrO$_2$	1.94	0.46	0.005	2.49	0.15	0.003	24.6
DC-20%Co/ZrO$_2$	1.95	0.53	0.012	2.50	0.50	0.006	48.5

Analysis of the EXAFS fitting data are illustrated in **Table 3** and **Figure S19**. The data shows the same trend as in the XANES data that the reduced DC samples have a higher degree of reduction compared to the D samples. The Co-O distance values (R) which relate to the residual oxide are similar for the dried and dried-calcined samples in each case except for the alumina where there is a significant difference (**Figure S19 (a)**). This could be due to the formation of CoO in the DC sample and probably a material with a stronger Co-O-Al interaction in the dried reduced sample. It is also worth mentioning that for the catalysts supported on reducible supports, the degree of reduction of the D samples is much higher than in the case of the non-reducible supports. This is

most probably the consequence of the reducible supports to promote the hydrogen spillover [53], hence promoting the reduction of the Co phase.

DRIFTS analysis. CO DRIFTS analysis was performed to establish the fcc:hcp ratio for individual samples. DRIFTS spectra for dried and dried-calcined samples consist of a wide absorption band with the maximum situated generally around 2040 cm^{-1} value. Most absorption bands present a clear shoulder towards the lower wavenumbers, or the shape is not symmetrical. However, the most interesting samples are those supported on ZrO_2 (**Figure 8**) because the dried only sample presents a CO absorption band that is symmetric, much narrower and centered at a lower wavenumber. Previous work [54] ascribed the absorption band at 2054 cm^{-1} to CO adsorbed on fcc Co, while the absorption band at 2035 cm^{-1} was ascribed to CO adsorbed on hcp Co. Prieto et. al. [55] also ascribed the absorption band at 2050 cm^{-1} to CO adsorbed on fcc Co, while the lower wavenumber shoulder was assigned to "low-coordinated surface sites located on more open low-index surface crystallographic planes or steps and corners", which is equivalent to stacking faults. Based on a previous study by Enache et al [9] which showed that directly reduced Co/ZrO_2 catalysts increase the amount of hcp Co at the expense of fcc Co, we assume that the same phenomenon happens here. Because D-Co/ZrO$_2$ sample (**Figure 8(a)**) presents virtually only hcp Co on the catalyst's surface, we could perform the deconvolution and split the contribution of the two types of metallic Co present on the samples. The deconvolution of the absorption bands was completed using Origin 9.1 software package, using a Gaussian peak fit curve and by keeping the FWHM value constant at 24.9667 throughout the study. This is different when compared with other studies, i.e. A.Paredes-Nunez et al. [56], which performed the deconvolution using a higher FWHM for the less intense absorption bands. We believe that it should be either equal, or that the ration of the

FWHM should be proportional to the ratio of the intensity of the absorption bands. The second deconvolution option would probably be the best, but it would be exceedingly difficult to perform. Based on the Co/ZrO_2 spectra, we also assumed the split between the absorption bands characteristic to fcc Co and hcp Co to be always 23 cm^{-1} and from this point onwards we used the same absorption band split for all the catalysts studied. The designation of the bands was made by trial and error for all the other samples, until we obtained a good fit between the experimental data and the simulation (designated as Cumulative spectrum). **Figure 8** and **Figure S20** present DRIFTs spectra and the deconvolution of the spectra of all other catalysts studied while the assignment of the absorption bands for the samples obtained on each support is displayed in **Table S1**. Some of the spectra presented in these figures (i.e. Figure 8 (b) and S 19 (c) and (e)) present a tailing towards the lower wavenumbers. This is due to the presence of CO adsorbed in the bridged form onto the metallic Co. This adds to the complexity of the spectra and making it unviable to have a quantitative analysis of fcc Co versus hcp Co between samples.
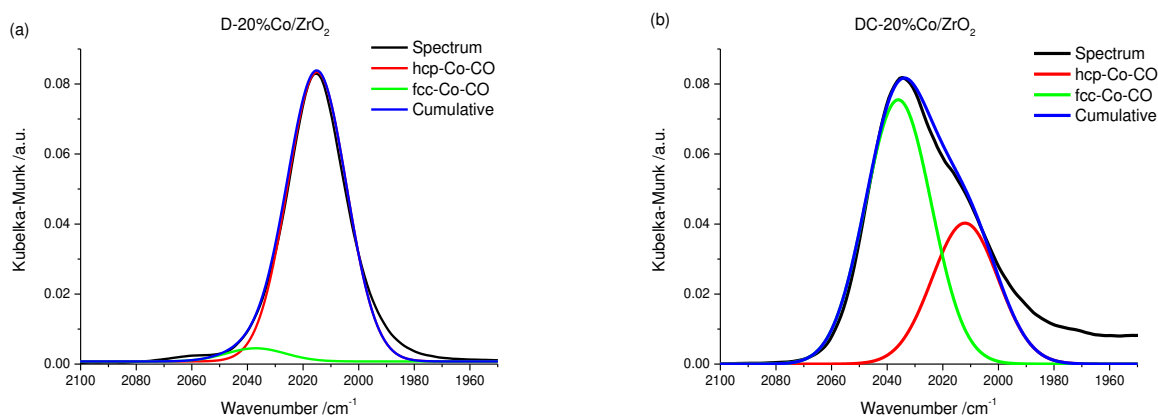
Figure 8. DRIFTS analysis of adsorbed CO onto D-20%Co/ZrO₂ (a) and DC-20%Co/ZrO₂ (b)

It might be argued that the assignment of the absorption bands to adsorbed CO onto fcc Co and hcp Co is not conclusive and that the shape is influenced by the presence of particles with various sizes. Based on the E(S)TEM data we presented above, all D samples present a narrow (mono-modal) particle size distribution of the Co particles. Therefore, if the position and shape of the Co-CO absorption band would be a function of the particle size, then we should get for all these samples a narrow absorption band, with no shoulder present. Moreover, the particle sizes of these samples supported on various supports ranges between 1.5 nm (for DC-20%Co/SiO$_2$) and 9.8 nm (for DC-20%Co/TiO$_2$). If the position and shape of the absorption band would be a function of the particle size of the samples, such a wide range would shift the position of the maximum absorption towards lower or higher wavenumbers. However, this is not what we observe in our study and the only possible explanation is that the deconvoluted absorption bands are the result of the CO adsorption onto fcc and hcp Co.

Table 4 presents the maximum intensities of the absorption bands for all the samples and gives the ratio of fcc to hcp on each of the samples. Except for the zirconia based catalysts, all other D samples present a higher absorption maximum compared with their DC equivalents. This suggests that the dried-only samples contain a higher number of sites capable for CO adsorption, probably partly because of the better dispersion they possess and partly by the generation of a larger number of low-coordination Co^0 sites [25], despite their lower degree of reduction. This is in excellent agreement with the ESTEM data presented in the preceding sections, which showed that for the samples of Co supported on silica and alumina the dispersion of the active phase is uniform and no large agglomerates of Co$_3$O$_4$ were observed. Even though the DC-Co/TiO$_2$ sample does not present large aggregates of Co$_3$O$_4$ and the distribution of Co appears to be uniform throughout, the particle size of the individual Co particles is 3 times that of the individual particles present in the sample D-Co/TiO$_2$ (**Figure S15**). This finding is reflected also in the DRIFTS analysis in **Table 4**, which shows a much-enhanced CO adsorption capability for the D sample. In the case of zirconia-supported

catalysts, the maximum intensity of the absorption band values measured for D and DC samples are almost identical, suggesting that the number of sites capable for CO adsorption is similar. This is again consistent with the ESTEM results, which showed that for titania and zirconia-supported catalysts large clumps of Co_3O_4 were not observed.

Table 4. Maximum intensities of the absorption bands over the samples and the fcc to hcp ratio.

Catalyst	Max. absorption band intensity	Max. fcc Co absorption intensity	Max. hcp Co absorption intensity	Ratio fcc:hcp
D-20%Co/SiO$_2$	0.4303	0.3795	0.3213	1.18
DC-20%Co/SiO$_2$	0.0616	0.0591	0.0411	1.44
D-20%Co/Al$_2$O$_3$	0.3059	0.2965	0.1843	1.61
DC-20%Co/Al$_2$O$_3$	0.1249	0.1203	0.0722	1.67
D-20%Co/TiO$_2$	0.3288	0.3143	0.1129	2.78
DC-20%Co/TiO$_2$	0.0515	0.0327	0.0365	0.90
D-20%Co/ZrO$_2$	0.0830	0.0045	0.0830	0.05
DC-20%Co/ZrO$_2$	0.0818	0.0752	0.0402	1.87

However, in the case of the Co/ZrO$_2$ the ratio fcc:hcp Co is very low. It therefore seems likely that the type of sites (Co hcp) generated by this treatment method are responsible for the change in activity (and not the increase in the number of sites capable of CO adsorption). (**Figure 9** and **Table 4**).
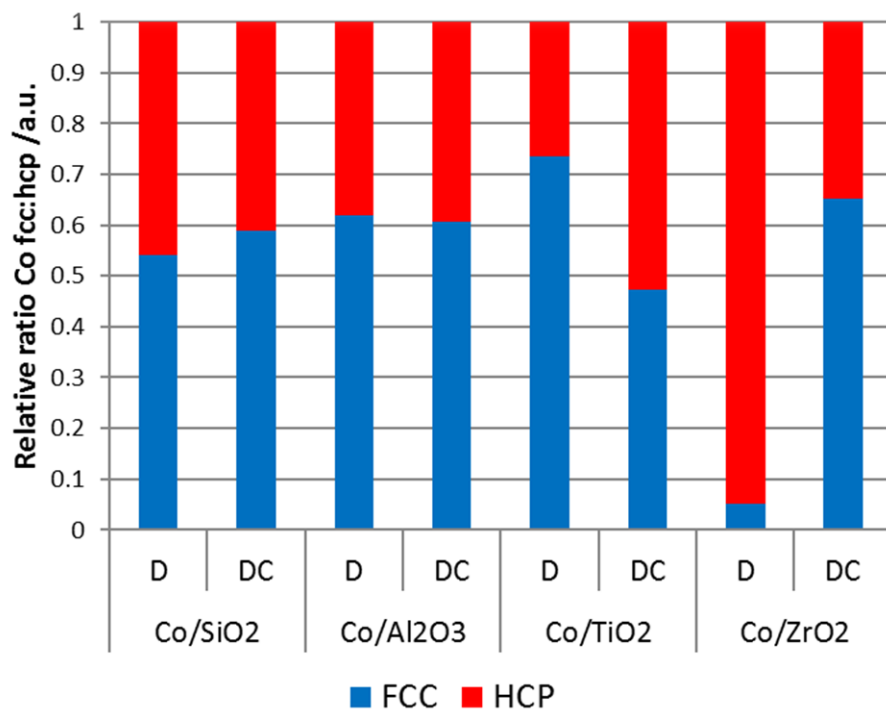
Figure 9: Relative ratio fcc : hcp in the different D and DC supported Co catalysts

DISCUSSION

The thermal history of the samples is of crucial importance for the performance displayed by the FT catalysts. In this study, we have presented evidence through dynamic ESTEM that the D-samples have a better dispersion of Co than the DC-samples for the catalysts on the different supports. The better dispersion of low coordination Co atomic species (single atoms and atomic clusters) and Co nanoscale particles with irregular surfaces revealed by dynamic E(S)TEM and a better hcp : fcc ratio of the particles correlate with the higher activity of the D samples (Tables 1 and 4).

For all of the samples shown in **Figure 6,** our direct observations illustrate that the removal of the calcination step results in smaller Co nanoparticles and a higher dispersion of Co species compared to their DC analogues. This provides a direct comparison with the results shown in **Figure 5** for the silica supported samples. The D samples consist of Co species smaller than that of the oxide agglomerates found in the calcined silica samples and in the DC-Co/Al$_2$O$_3$ sample. This indicates that removal of the calcination procedure creates a higher dispersion of the metallic active phase; whereas inclusion of the calcination procedure tends to sinter the Co species and therefore reduce their active surface area.

Previous studies have suggested that the ideal Co particle size range for FT catalysts is between 6-8 nm, as the limited geometry of smaller particles reduces the concentration of active sites upon which reaction can occur,[6, 7]. However, our dynamic E(S)TEM data reveal the presence of single atoms of Co and clusters and nanoparticles of Co with irregular surfaces under the reduction reaction conditions, consistent with reports that low coordination sites are likely to be important in FT activity [25,29].

CO is not only the probe molecule employed in the DRIFTS analysis to study the surface amounts of fcc and hcp Co, but also it is one of the reagents in the FT synthesis. Gas-phase (free) CO [57] presents two absorption bands at 2174 and 2120 cm^{-1} respectively. Adsorbed CO onto fcc Co shows an absorption band at about 2040 cm^{-1} for our samples, and that the C-O bond strength is reduced when compared with the free CO case. In the case of the CO adsorbed onto hcp Co, the maximum of the absorption band of is further shifted to even lower values (2010-2020 cm^{-1} depending on the support), demonstrating that the C-O bond is further weakened and therefore easier to break and achieve the CO dissociation. This study enabled us to monitor the ratio of fcc and hcp Co as a function of the thermal treatment, but it also put in evidence that for the catalysts

supported on silica, alumina and titania, the number of sites capable of CO adsorption was enhanced by the removal of the calcination step. This finding agrees with the ESTEM data, which showed the absence of large agglomerates of Co_3O_4 for the directly-reduced samples, in contrast with the samples that were submitted to a calcination step.

Comparisons of data in **Table 1** and **Table 4**, generally show that the relative activity of the catalysts is influenced by both the dispersion (number of active sites) and the hcp Co : fcc Co ratio. In the case of the catalysts supported on zirconia (D-Co/ZrO_2), the DRIFTS results indicated that there was no substantial increase in the number of sites capable of adsorbing CO, but an almost complete generation of Co hcp sites, at the expense of the fcc Co at the surface of the active phase. This is again consistent with the initial ESTEM data for the dispersion of Co particles for both the D and DC samples for this system. Zirconia is sometimes used as an activity promoter in FT catalysts [58]. Although we did not synthesize, test or characterize such samples, we speculate that such systems work probably due to the result of increasing the amount of hcp Co in the surface of the active phase and the generation of sites capable of hydrogen spillover, compared with the unpromoted case.

On non-reducible supports, the degree of reduction (DOR) of the D-samples is very low (described in the XANES/EXAFS results in the preceding sections). The DOR of DC-Co/SiO_2 is higher than that of DC-Co/Al_2O_3 because of the stronger metal-support interactions in the case of the alumina-based catalyst. However, the dispersion is greatly improved in the case of D samples: Co_3O_4 agglomerates are not present in the ESTEM images of D catalysts, as opposed to the images acquired for the DC samples. Finally, DRIFTS revealed a substantially enhanced number of sites capable of adsorbing CO are present in the case of dried-reduced catalyst.

In the case of reducible supports, the degree of reduction of the D-samples is improved, compared with the DOR of the DC-Co/Al$_2$O$_3$ and even DC-Co/SiO$_2$. We believe this to be due to the presence of highly reactive spillover hydrogen species, capable of reducing the cobalt precursor to a higher extent. However, the corresponding DC samples supported on reducible supports still present a higher degree of reduction when compared with the dried-only samples. ESTEM revealed greatly improved dispersion in the case of D-Co/TiO2 when compared with DC-Co/TiO$_2$. That result was also confirmed by the amount of CO adsorbed via the DRIFTS analysis. In the case of zirconia-supported materials, ESTEM showed a greater level of dispersion of Co species in the dried-reduced sample compared to the dried-calcined-reduced sample. The DRIFTS results indicated a similar number of sites capable of adsorbing CO for both D and DC zirconia catalysts. It seems likely that the increase in the activity of the D-Co/ZrO$_2$ compared to the DC-Co/ZrO$_2$ is due to the increased number of hcp Co nanoparticles on the support compared to the DC sample in this system (**Figure 9** and **Table 1**).

SUMMARY AND CONCLUSION

In conclusion, the dried-reduced samples are always more active than the dried-calcined-reduced alternatives, irrespective of the support employed with no change to the selectivity values. Based on the systematic data presented in this study, the authors conclude that the increase in activity measured for D versus DC samples is due to a combination of better dispersion of Co active species and/or a higher hcp:fcc ratio. The calcination process results in large particles and agglomerates of cobalt oxide species which reduce the amount of active sites available for CO adsorption. By removing the calcination process, the activity of supported catalysts improves, especially for those prepared on reducible supports. However, the non-reducible supports promote more highly

dispersed small Co metal species (including atomic clusters and single atoms of the catalysts observed in the dynamic ESTEM) leading to more active sites for CO adsorption in FT synthesis.

AUTHOR INFORMATION

*Corresponding authors:

*Email for PLG: pratibha.gai@york.ac.uk

*Email for EDB: ed.boyes@york.ac.uk

*Email for DE: dan.enache@matthey.com

ORCID

Pratibha L. Gai: 0000-0003-3837-7148

Edward D Boyes: 0000-0001-8456-1208

Peter R. Ellis: 0000-0002-2806-7915

ASSOCIATED CONTENT

Supporting information (SI)

The supporting information is available free of charge on the ACS Publications website.

Additional information regarding the experimental methods and data analysis (PDF).

References

(1) King, D.L.; De Klerk, A. Overview of Feed-to-Liquid (XTL) Conversion. *ACS Symposium Series*. 2011, 1084, 1-24.

(2) Fischer, F.; Tropsch, H. Process for the production of paraffin-hydrocarbons with more than one atom. Patent US 1746464 A, 1925.

(3) Zhang, Q.; Cheng, K.; Kang, J.; Deng, W.; Wang, Y., Fischer–Tropsch Catalysts for the Production of Hydrocarbon Fuels with High Selectivity. ChemSusChem. 2014, 7**,** 1251-1264.

(4) Iglesia, E. Design, synthesis, and use of cobalt-based Fischer-Tropsch synthesis catalysts. Appl. Catal. A 1997, 161, 59-78.

(5) Munnik, P.; de Jongh, P. E.; de Jong, K. P. Control and Impact of the Nanoscale Distribution of Supported Cobalt Particles Used in Fischer-Tropsch Catalysis. J. Am. Chem. Soc. 2014, 136**,** 7333-7340.

(6) Wolters, M.; Munnik, P.; Bitter, J. H.; de Jongh, P. E.; de Jong, K. P. How NO Affects Nickel and Cobalt Nitrates at Low Temperatures To Arrive at Highly Dispersed Silica-Supported Nickel and Cobalt Catalysts. J. Phys. Chem. C 2011, 115, 3332-3339.

(7) Wang, B.; Chen, J.-F.; Zhang, Y. Synthesis of highly dispersed cobalt catalyst for hydroformylation of 1-hexene. RSC Advances 2015, 5, 22300-22304.

(8) Navarro, V.; van Spronsen, M. A.; Frenken, J. W. M. In situ observation of self-assembled hydrocarbon Fischer–Tropsch products on a cobalt catalyst. Nat Chem. 2016, 8, 929-934.

(9) Enache, D. I.; Rebours, B.; Roy-Auberger, M.; Revel, R. *In Situ* XRD Study of the Influence of Thermal Treatment on the Characteristics and the Catalytic Properties of Cobalt-Based Fischer–Tropsch Catalysts. J. Catal. 2002, 205**,** 346-353.

(10) du Plessis, H. E.; Forbes, R. P.; Barnard, W.; Erasmus, W. J.; Steuwer, A. *In situ* reduction study of cobalt model Fischer–Tropsch synthesis catalysts. Phys. Chem. Chem. Phys. 2013, 15**,** 11640-11645.

(11) Høydalsvik, K.; Fløystad, J. B.; Voronov, A.; Voss, G. J. B.; Esmaeili, M.; Kehres, J.; Granlund, H.; Vainio, U.; Andreasen, J. W.; Rønning, M.; Breiby, D. W. Morphology Changes of Co Catalyst Nanoparticles at the Onset of Fischer−Tropsch Synthesis. J. Phys. Chem. C 2014, 118**,** 2399-2407.

(12) Cats, K. H.; Weckhuysen, B. M. Combined Operando X-ray Diffraction/Raman Spectroscopy of Catalytic Solids in the Laboratory: The Co/TiO$_2$ Fischer–Tropsch Synthesis Catalyst Showcase. ChemCatChem. 2016, 8, 1531-1542.

(13) Kistamurthy, D.; Saib, A. M.; Moodley, D. J.; Niemantsverdriet, J. W.; Weststrate, C. J. Ostwald ripening on a planar Co/SiO$_2$ catalyst exposed to model Fischer–Tropsch synthesis conditions. J. Catal. 2015, 328, 123-129.

(14) Lancelot, C.; Ordomsky, V. V.; Stéphan, O.; Sadeqzadeh, M.; Karaca, H.; Lacroix, M.; Curulla-Ferré, D.; Luck, F.; Fongarland, P.; Griboval-Constant, A.; Khodakov, A. Y. Direct Evidence of Surface Oxidation of Cobalt Nanoparticles in Alumina-Supported Catalysts for Fischer−Tropsch Synthesis. ACS Catal. 2014, **4,** 4510-4515.

(15) Dehghan, R.; Hansen, T.; Wagner, J.; Holmen, A.; Rytter, E.; Borg, Ø.; Walmsley. In-Situ Reduction of Promoted Cobalt Oxide Supported on Alumina by Environmental TEM. J. Catal. Lett. 2011, 141, 754-761.

(16) Xin, H. L.; Pach, E. A.; Diaz, R. E.; Stach, E. A.; Salmeron, M.; Zheng, H. Revealing Correlation of Valence State with Nanoporous Structure in Cobalt Catalyst Nanoparticles by In Situ Environmental TEM. ACS Nano 2012, 6, 4241-4247.

(17) Ward, M. R.; Boyes, E. D.; Gai, P. L. In Situ Aberration-Corrected Environmental TEM: Reduction of Model Co$_3$O$_4$ in H$_2$ at the Atomic Level. ChemCatChem. 2013, 5, 2655-2661.

(18) Rytter, E.; Tsakoumis , A.; Holmen, A. On the selectivity to higher hydrocarbons in Co-based Fischer–Tropsch synthesis. Catal. Today 261, 3 - 16.

(19) Senecal, P.; Jacques S.; Di Michiel, M.; Kimber, S.A.; Vamvakeros. A.; Odarchenko, Y.; Lezcano-Gonzale, I.; Paterson, J.; Ferguson, E.; Beale, A. Real-Time Scattering-Contrast Imaging of a Supported Cobalt-Based Catalyst Body during Activation and Fischer−Tropsch Synthesis Revealing Spatial Dependence of Particle Size and Phase on Catalytic Properties. ACS Catal. 2017, 7, 2284-2293.

(20) Pearson, W. B., A Handbook of Lattice Spacings and Structures of Metals and Alloys, Pergamon Press: New York, 1958; Vol. 4, p 500-503.

(21) Bezemer, G. L.; Bitter, J. H.; Kuipers, H. P. C. E.; Oosterbeek, H.; Holewijn, J. E.; Xu, X.; Kapteijn, F.; van Dillen, A. J.; de Jong, K. P. Cobalt Particle Size Effects in the Fischer-Tropsch Reaction Studied with Carbon Nanofiber Supported Catalysts. J. Am. Chem. Soc. 2006, 128, 3956-3964.

(22) Banerjee, A.; Navarro, V.; Frenken, J. W. M.; van Bavel, A. P.; Kuipers, H. P. C. E.; Saeys, M. Shape and Size of Cobalt Nanoislands Formed Spontaneously on Cobalt Terraces during Fischer−Tropsch Synthesis. The Journal of Physical Chemistry Letters 2016, 7, 1996-2001.

(23) Cook, K. ; Perez, H.; Bartholomew, C.; Hecker, W. Effect of promoter deposition order on platinum-, ruthenium-, orrhenium-promoted cobalt Fischer–Tropsch catalysts. Applied Catalysis A: General 2014, 482, 275-286.

(24) Shimura, K.; Miyazawa, T.; Hanaoka, T.; Hirata, S. . Fischer–Tropsch synthesis over alumina supported cobalt catalyst:Effect of promoter addition. Applied Catal. A: General. 2015, 494, 1-11.

(25) Prieto G.; Concepción P., Murciano R., Martínez A. The impact of pre-reduction thermal history on the metal surface topology and site-catalytic activity of Co=SiO2 Fischer–Tropsch catalysts. J. Catal. 2013, 302, 37-48.

(26) Gnanamani M.K.; Jacobs G., Shafer W.D., Davis B.H. Fischer–Tropsch synthesis: Activity of metallic phases of cobalt supported on silica. Catalysis Today 2013, 215, 13-17.

(27) Karaca, H.; Safonova, O.V.; Chambrey, S.; Fongarland, P.; Roussel, P.; Griboval-Constant A.; Lacroix M.; Khodakov A.Y. Structure and catalytic performance of Pt-promoted alumina-supported cobalt catalysts under realistic conditions of Fischer–Tropsch synthesis. J.Catal. 2011, 277, 14-26.

(28) Ducreux O.; Rebours B., Lynch J.; Roy-Auberger M.,; Bazin D. Microstructure of Supported Cobalt Fischer-Tropsch Catalysts. Oil&Gas Science and Technology –Rev IFP. 2009, 64, 49-62.

(29) Morales, F.; de Groot, F.M.; Visser, T.; Wekhuysen, B.M. Effects of manganese oxide promoter on the CO and H2 adsorption properties of titania-supported cobalt Fischer–Tropsch catalysts. J. Catal. 2007, 246, 91-99.

(30) Liu, J.X,.; Su. H.Y,.;Sun, D.P,.;Zhang, B.Y. Crystallographic Dependence of CO Activation on Cobalt Catalysts: HCP versus FCC. J.Am.Chem. Soc. 2013, 135, 16284-16285.

(31) van Santen, R.A.; Markvoort A.; Filot, I.A.; Ghouri, M.; Hensen, E.J. Mechanism and micro-kinetics of the Fischer–Tropsch reaction. PCCP. 2013, 15, 17038-17063.

(32). Lynch, J. Development of Structural Characterisation Tools for Catalysts. Oil Gas Sci. Technol. 2002, **57**, 281–305.

(33) Patanau E. The impact of sequential H2-CO-H2 activation treatment on the structure and performance of cobalt based catalysts for the Fischer-Tropsch synthesis. Appl Catal A (General) 2018, 549, 208-288.

(34) Gai, P. L.; Boyes, E. D. Advances in *in-situ* atomic resolution-environmental transmission electron kcroscopy (ETEM) and 1Angstrom aberration corrected electron microscopy. Microsc. Res. Tech., 2009, 72, 153-164.

(35) Boyes, E. D.; Ward, M. R.; Lari, L.; Gai, P. L. ESTEM imaging of single atoms under controlled temperature and gas environment conditions in ctalyst reaction studies. Ann. Phys. (Berlin). 2013, 525, 423-429.

(36) Boyes, E. D.; Gai, P. L. Visualising reacting single atoms under controlled conditions: Advances in atomic resolution in situ Environmental (Scanning) Transmission Electron Microscopy (E (S)TEM). Comptes Rendus Phys. 2014, 15, 200-213.

(37) Boyes, E.D. ; Gai, P.L. Visualizing reacting single atoms in chemical reactions: Advancing the frontiers of materials research. MRS Bull. 2015, 40, 600-604.

(38) Gai, P.L.; Lari, L.; Ward, M.R.; Boyes, E.D. Visualiation of single atom dynamics and their role in nanocatalysis under controlled reaction environments. Chem.Phys.Lett. 2014, 592, 355-359.

(39) Boyes, E.D.; Gai, P.L. Environmental high rsolution electron microscopy and applications to chemical science. Ultramicroscopy 1997, 67, 219-229.

(40) Gai, P.L.; Kortakis K. Solid staate defect mechanism in vanadyl pyrophoshate: implications for selective oxidation. Science 1995, **2**67, 661-663.

(41) Gai, P.L.; Boyes, E.D.; Hansen, P.; Helveg, S;. Giorgio, S.; Henry, C.; Atomic Resolution Environmental transmission electron microsopy for probing gas-solid reactions in heterogeneous catalysis. MRS Bull. 2007, 32, 1044-1048.
.
(42) Lagrow, A.P.; Lloyd, D.C.; Gai, P.L.; Boyes, E.D. Visualizing the Cu/Cu_2O Interface Transition in Nanoparticles with Environmental Scanning Transmission Electron Microscopy (ESTEM). Jounal of American Chemical Society 2017, 139, 179-185.

(43) Siju, N.R.; Yoshida, K.; Boyes, E.D.; Brown, D.; Gai, P.L. Dynamic atomic scale *in situ* electron microscopy in the development of an efficient heterogeneous catalytic process for pharmaceutical NSAIDS. Catal.Sc.Technol. 2011, 1, 413-425.

(44) Gai, P.L.; Yoshida, K.; Ward, M.R.; Walsh,M.; Van der Water L.; Baker R.T.; Watson, M.J.; Boyes, E.D. Visualisation of single atom dynamics in water gas shift reaction for hydrogen generation. Catal.Sc.Technol. 2016, **6**, 2212-2227.

(45) Ward, M.R.; Theobald, B.; Sharman, J.; Boyes, ED.; Gai, P.L. Direct observations of dynamic PtCo interactions in fuel cell catalyst precursors at the atomic level using E (S) TEM. J. Microscopy 2018, 269, 143-150.

(46) Gai, P.L. Direct probing of gas molecule–solid catalyst interactions on the atomic scale. Advanced Materials 1998, 10, 1259-1263.

(47) Gai, P.L.; Boyes, E.D. Electron Microscopy of heterogeneous catalysts. IOP Publ.; Bristol and Philadelphia, 2003.

(48) Gai, P.L.; Boyes, E.D. Atomic Resolution-ETEM*: in Handbook of Nanoscopy; 1st ed.; Van Tendeloo, G.; Van Dyck, D.; Pennycook, S.J., Eds.; Wiley-VCH: Verlag GMBH & Co KGaA, Germany, 2012*, Vol. 1, p. 375-403.

(49) Reuel, R.C.; Bartholomew, C.H. The stoichiometries of H_2 and CO adsorptions on cobalt: Effects of support and preparation. J. Catal. 1984, 85, 63-77.

(50). Ravel, B.; Newville, M. ATHENA, ARTEMIS, HEPHAESTUS: data analysis for X-ray absorption spectroscopy using IFEFFIT. J. Synchrotron Radiat. 2005, 12, 537–541.

(51) Karim W.; Spreafico C.; Kleibert A.; Gobrecht J.; VandeVondele J.; Ekinci Y.;van Bokhoven J.A.. Catalyst support effects on hydrogen spillover. Nature 2017, 54, 68-71.

(52) Argyle, M.D.; Frost, T.S.; Bartholomew, C.H. Cobalt Fischer–Tropsch Catalyst Deactivation Modeled Using Generalized Power Law Expressions. Tops. Catal. 2014, 57, 415-429.

(53) Prins, R. Hydrogen Spillover. Facts and Fiction. Chem Rev. 2012, 112 , 2714-2738.

(54) Song, D.; Li, J.; Cai, Q. In Situ Diffuse Reflectance FTIR Study of CO Adsorbed on a Cobalt Catalyst Supported by Silica with Different Pore Sizes. J.Phys.Chem. C 2007, 111 18970-18979.

(55). Prieto, G.; Martinez, A.; Concepcion, P.; Moreno-Tost, R. Cobalt particle size effects in Fischer–Tropsch synthesis: structural and in situ spectroscopic characterisation on reverse micelle-synthesised Co/ITQ-2 model catalysts. J. Catal. 2009, 266, 129-144.

(56).   A.Paredes-Nunez; D.Lorito; Y.Schuurman; N.Guilhaume; F.C.Meunier, Origins of the poisoning effect of chlorine on the CO hydrogenation activity of alumina-supported cobalt monitored by operando FT-IR spectroscopy, J. Catal. 2015, 329, 229-236.

57. http://webbook.nist.gov/cgi/cbook.cgi?ID=C630080&Type=IR-SPEC&Index=0#IR-SPEC

58. Hong, J.; Chu, W.; Chernavskii, P.; Khodakov, A.Y. Effects of zirconia promotion on the structure and performance of smaller and larger pore silica-supported cobalt catalysts for Fischer–Tropsch synthesis. Appl.Catal. A General 2010, 382, 28-35.

.